CHAPTER 4

Application of Computational Methods to Supported Metal–Oxide Catalysis

THOMAS P. SENFTLE,[a] ADRI C.T. VAN DUIN[b] AND MICHAEL J. JANIK*[c]

[a] Department of Chemical Engineering, Pennsylvania State University, University Park, PA 16802, USA; [b] Department of Mechanical and Nuclear Engineering, Pennsylvania State University, University Park, PA 16802, USA; [c] Department of Chemical Engineering, Pennsylvania State University, University Park, PA 16802, USA
*Email: mjanik@engr.psu.edu

4.1 Introduction

Heterogeneous catalysts featuring metal particles dispersed on an oxide support play an indispensable role in numerous industrial chemical processes. The petrochemical industry relies on supported metal–oxide catalysts for processes that generate industrial chemical feedstocks by reforming the useful byproducts of fossil fuel refinement. Furthermore, many clean energy technologies rely on supported metal–oxide catalysts for the treatment of combustion exhaust and for high-temperature fuel cell applications. Examples of supported metal–oxide catalysis include: catalytic combustion,[1–12] hydrocarbon steam-reforming,[13–24] CO removal from *syngas via* the water–gas-shift (WGS) reaction,[25–34] CO and NO oxidation,[35–41] automotive three-way catalysis,[42–46] solid oxide fuel cell (SOFC) electrodes,[47–53] and selective hydrogenation.[54–59] The activity and

selectivity of supported metal–oxide catalysts can be tuned for these applications by altering the metal–support surface morphology.[60]

The computational methods presented in this book can complement experimental efforts in building a molecular level understanding of supported metal–oxide catalysis. Identifying stable surface morphologies, active surface sites, and reaction mechanisms is a difficult task owing to the complexity of competing factors influencing the behavior of the catalyst.[61] To name a few variables, catalyst activity and stability are directly linked to the size and distribution of the metal particles on the oxide surface,[62–64] the oxidation state of the metal,[65–67] charge transfer between the particle and the support,[68–71] the electronic structure of the metal–oxide interface,[70,72–76] the concentration of oxygen-vacancies on the oxide surface,[77–79] the formation of metal–oxide surface phases,[80–83] the incorporation of metal atoms in oxide lattice positions,[4,69,78,84–89] and adsorbate coverage effects.[90–93] Furthermore, these effects are highly dependent on variable reaction conditions: namely, gas phase partial pressures and temperature. A fundamental understanding of how these phenomena are linked to catalytic behavior is essential for making informed design decisions that will yield stable and active catalysts.

This chapter will highlight examples from the literature that apply DFT, *ab initio* thermodynamics, and empirical force-field methods to assess catalytic behavior of supported metal–oxide catalysts. Section 4.2 will provide a brief overview of these computational methods as they pertain to supported metal–oxide systems. Section 4.3.1 considers studies that apply DFT to the design of water–gas-shift catalysts, evaluating the relative energies of metal–oxide surface structures and mapping reaction mechanisms. Section 4.3.2 discusses studies that extend the formalism of DFT to non-zero temperature and pressure *via ab initio* thermodynamics, thus assessing the impact of surface stability on catalytic behavior. Section 4.3.3 focuses on studies that use ReaxFF empirical force-fields in molecular dynamic (MD) and Monte Carlo (MC) simulations to investigate system dynamics at larger time and length scales. Section 4.3.4 highlights initial and ongoing multi-scale studies that integrate the above methods to characterize Pd/ceria catalysts.

4.2   Computational Approaches to Supported Metal–Oxide Catalysis

Advances in computational chemistry over the last few decades have had a great impact on design strategies for obtaining active, selective, and stable catalysts.[94] In particular, density functional theory (DFT)[95–98] has shown tremendous success in modeling catalytic systems, thus enabling *a priori* approaches to designing metal–oxide catalysts. DFT is capable of determining the electronic ground state energy of a system as a function of atomic positions. Thus, one can determine the optimized structure of the catalyst surface during every step of a reaction – allowing determination of stable intermediates and activation barriers on the potential energy surface (PES) of a reaction

coordinate. The computational expense of DFT, however, limits system sizes to around ~ 100 atoms. For this reason, it is often limited to periodic models of single crystal surfaces, which are used to represent the varying surface facets of large particles. Furthermore, characterizing the interactions between a metal cluster and an oxide support requires highly idealized models, featuring perfectly dispersed metal atoms and clusters, that can only approximate the behavior of actual catalytic systems. Despite this limitation, DFT has proved instrumental for mapping reaction mechanisms and evaluating particle–support interactions at the electronic level.

Reaction conditions, dictated by the temperature and partial pressure of gaseous species, affect the stability and reactivity of the catalyst surface. Understanding this effect is necessary to identify surface phases that are stable and active under *reaction conditions*. As a quantum theory, DFT does not inherently account for the effects of temperature and pressure. DFT can be extended to treat systems at realistic temperatures and pressures through the formalism of *ab initio* thermodynamics.[79,82,98–102] *Ab initio* thermodynamics uses statistical mechanics to incorporate the effect of entropy in systems where solid catalyst surfaces are in equilibrium with a molecular gas phase. This method can calculate the *free energy* of a system, therefore allowing one to determine the relative *stability* of possible surface terminations and structures. With this information, one can construct phase diagrams predicting morphologies that will dominate the catalyst surface as a function of temperature and pressure.

Sufficient models of metal–support structures and dynamics are often beyond the length and time scales that are computationally tractable with DFT. This has provided the impetus to employ classical force-fields, such as the ReaxFF,[103] that are empirically derived from quantum and experimental data. The classical basis for empirical potentials allows for the computational treatment of systems reaching the order of $\sim 10^4$ atoms for nanosecond timescales, which is sufficient to capture system *dynamics* through MD and MC simulations. The application of reactive force-field methods to heterogeneous catalysis is an emerging research area. Herein we highlight the applications of ReaxFF to heterogeneous catalysis over metal and oxide surfaces. The success of these studies has led to ongoing attempts to apply this method to supported metal–oxide systems.

4.3 Selected Applications

The following sections highlight studies employing the computational methods discussed in the previous section to characterize supported metal–oxide systems. It is not intended to be an exhaustive review of the subject, but rather serves to illustrate the strengths and limitations of these methods when applied to supported heterogeneous catalysis. It is broken into three sections corresponding to DFT applied to water–gas-shift (WGS) catalysis (4.3.1), applications of *ab initio* thermodynamics to assess thermodynamic stability of surfaces (4.3.2), and applications of empirical force-fields (4.3.3). The sections

are organized to highlight the individual capabilities of each method, and we have therefore restricted our discussion of each study to the components most directly related to the specific method under consideration. In fact, many of the studies discussed herein apply these methods together, and we ask the reader to keep this in mind as these extensions are not always discussed explicitly. An example of these methods applied in tandem will be discussed in the final section.

The studies discussed in this chapter are chosen to illustrate the capabilities and limitations of computational methods applied to supported metal–oxide catalysis. This chapter is not intended as a comprehensive review of the subject and, as such, numerous notable studies are not discussed in detail. We would nevertheless like to summarize quickly a few especially notable studies before moving to more detailed discussions.

Oxidation of CO is an important industrial process, and has been the subject of many computational studies. Notable contributions have been made by Landman and coworkers, who applied DFT in conjunction with isotopic labeling experiments to determine the oxidation state of Pd clusters supported on MgO during CO oxidation.[104] This allowed them to determine that partially oxidized Pd clusters are active toward CO oxidation, along with the temperature range in which the clusters will remain oxidized. In another study, these authors used quantum (QM) calculations in tandem with infrared spectroscopy to demonstrate that charging effects lead to enhanced CO oxidation activity over Au/MgO catalysts. They show that this charging effect is prominent when Au clusters are adsorbed on oxygen-vacancy defects and is absent in clusters adsorbed on the pristine oxide.[105] Hammer, Molina, and coworkers demonstrate that oxide supports can play an active role in reaction mechanisms in their DFT work analyzing CO oxidation over Au/MgO.[106] They demonstrate the importance of interfacial sites and charge transfer between the oxide support and the metal cluster, which leads to enhanced CO oxidation activity over Au/TiO$_2$.[107]

The interaction between supported metal clusters and adsorbed hydrogen plays a prominent role in many catalytic processes, such as selective hydrogenation, dehydrogenation, and water–gas-shift. Vayssilov, Rösch, and coworkers used DFT to explore hydrogen saturation on supported Ir, Rh, and Pt clusters.[108,109] They found that the extent of hydrogen uptake is dependent on metal type, and is enhanced in metals that are easily oxidized by the support. Sautet and coworkers conducted multiple studies that investigate structural changes to Pt and Pd clusters adsorbed on γ-alumina caused by hydroxyl groups and H$_2$.[110,111] Using *ab initio* thermodynamics, they found that in a hydrogen-free atmosphere Pt clusters prefer to adsorb on the oxide in a planar configuration. They subsequently showed that the Pt cluster undergoes reconstruction to a cuboctahedral structure after exposure to hydrogen, induced by the formation of a metal hydride. This restructuring occurs above a critical hydrogen pressure, and greatly affects the catalytic properties of the system. These studies underscore the need to consider interactions between metal clusters and oxide surfaces when assessing catalytic behavior. This type of

analysis is exemplified in the work of Ferrando, Fortunelli, Barcaro, and coworkers who use QM-global optimization methods to model the metal adsorption on oxides.[112–114]

4.3.1 Application of DFT to WGS

DFT is a powerful method for determining reaction mechanisms over metal–oxide systems. We have chosen to review studies that focus on developing catalysts for the water–gas-shift reaction because this is a particularly active research area with numerous examples of DFT application to supported metal–oxide catalysis. The studies first considered herein assess the activity of unsupported gold and copper metal clusters, which can then be compared directly to studies over the analogous oxide-supported systems. The importance of considering particle–support interactions is emphasized, because the oxide support can often play an active role in catalytic mechanisms.

4.3.1.1 *Supported Metal–Oxide Catalysts for Water–Gas Shift*

There is a growing interest in the production of pure H_2 for use in proton exchange membrane (PEM) fuel cell applications.[34] Typical H_2 production methods implement steam-reforming techniques that convert hydrocarbon feedstocks to a synthesis gas mixture of CO, H_2O, CO_2, and H_2. However, CO is detrimental to the efficiency of PEM fuel cells because it poisons the anode catalyst. For this reason, it is essential to remove CO in a downstream process between the steam-reforming and PEM stages. The water–gas-shift (WGS) reaction removes CO and recovers its energy content in a single process by converting CO and H_2O to CO_2 and usable H_2:

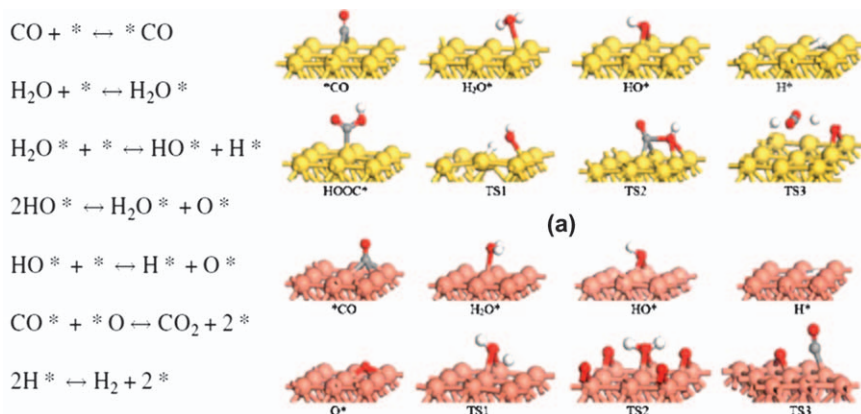$$CO_{(g)} + H_2O_{(g)} \rightarrow CO_{2(g)} + H_{2(g)} \tag{4.1}$$
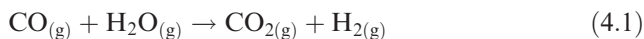
Recent DFT studies have characterized the nature of active sites on metal–oxide catalysts for WGS, which emphasize the unique aspects of particle–support interactions in Cu/ceria,[115] Au/ceria systems,[116] and Pt/ceria[117] (among numerous others). The primary intent of this section is to exhibit the utility and limitations of DFT for investigating the many aspects of metal–oxide catalysis, rather than to serve as an exhaustive review of computational work on WGS catalysis in the literature. For a more detailed discussion of the subject, we refer the reader to the recent review of computational work on Au/ceria that can be found in a perspective article by Zhang, Michaelides, and Jenkins.[118]

### 4.3.1.2 *Activity of Au and Cu Nanoparticles*

Liu, Rodriguez, and coworkers[115,116,119] applied DFT methods together with experimental studies to investigate how particle–support interactions affect the WGS activity of Au and Cu nanoparticles supported on reducible oxides, such

as ceria and titania. With DFT, the authors calculated reaction energies and activation barriers over unsupported Au and Cu particles.[119] They then compared the activity of Au and Cu particles supported on CeO_2 and ZnO substrates.[115] Their experimental evidence suggests that Au supported on CeO_2 is highly active despite the low activity of both metallic and ZnO supported Au clusters. This contrast suggests that particle–support interactions in CeO_2 supported catalysts play a critical role activating metal clusters for WGS. Computational methods have elucidated the unique behavior of Au/CeO_2 not present on Au/ZnO or unsupported Au-clusters. To accomplish this, the authors utilized DFT methods to evaluate candidate reaction mechanisms by locating optimized intermediate and transition structures on the potential energy surface.

To better understand the effect of the oxide support, the authors first study the activity of unsupported particles in the gas phase. The authors constructed model Au and Cu particles consisting of 29 atoms in a pyramidal geometry, whose shape and size are consistent with those observed by scanning tunneling microscopy[120] and X-ray diffraction.[121] Once the reaction energetics over unsupported particles are understood, they can be directly compared to energetics over the same particles supported on an oxide substrate. The catalytic performance of clean Au(100) and Cu(100) surfaces was also evaluated for comparison against the performance of the nanoparticles. This provides a basis for assessing the importance of edge and corner sites in the reaction mechanism. The authors investigated two reaction mechanisms. The first is a redox mechanism, shown in Figure 4.1, which features the oxidation of the metal surface by the adsorption of CO and H_2O, followed by a subsequent surface reduction as adsorbed O atoms combine with CO before desorbing as CO_2. The second is an associative mechanism that proceeds through either formate or carboxyl surface intermediates. The optimized structures and corresponding reaction energy diagrams for these mechanisms are shown in Figures 4.1 and 4.2.

$$CO + * \leftrightarrow *CO$$

$$H_2O + * \leftrightarrow H_2O*$$

$$H_2O* + * \leftrightarrow HO* + H*$$

$$2HO* \leftrightarrow H_2O* + O*$$

$$HO* + * \leftrightarrow H* + O*$$

$$CO* + *O \leftrightarrow CO_2 + 2*$$

$$2H* \leftrightarrow H_2 + 2*$$

Figure 4.1   WGS redox reaction mechanism (left) and structures (right). (Adapted with permission from ref. 119 Copyright 2007 American Institute of Physics)
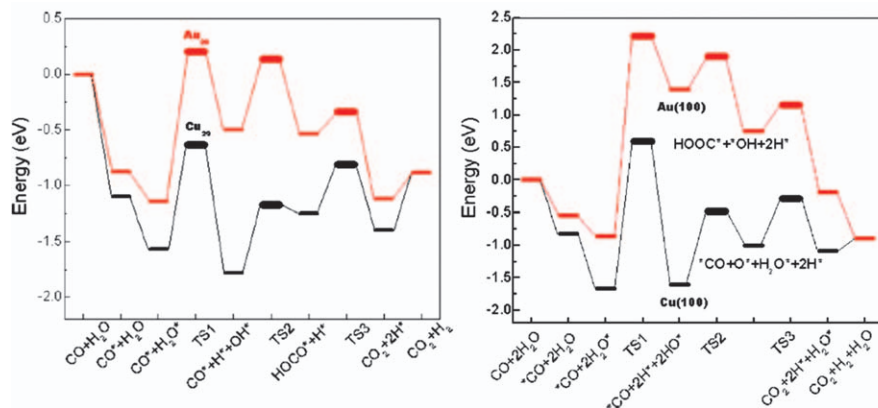
Figure 4.2 DFT energies for WGS reaction path over Au and Cu nanoparticles (left) and surfaces (right), demonstrating that lower energy paths are available over Cu catalysts compared to Au in the absence of support effects). (Adapted with permission from ref. 119 Copyright 2007 American Institute of Physics)

DFT allowed the authors to compare the energetic favorability of the possible mechanisms, thus identifying the likely reaction path over different catalytic surfaces. Cu(100) favors the redox mechanism, while the Au(100) surface (as well as the unsupported Au_{29} and Cu_{29} clusters) favors the associative mechanism. The reaction energy diagrams shown in Figure 4.2 further suggest that the rate-limiting step for the WGS reaction is the dissociation of adsorbed water for mechanisms over both Au and Cu. Determining the magnitude of the reaction barrier for the rate-limiting step allowed the authors to estimate the relative reaction rates over the varying catalytic surfaces. These results show that Cu is consistently more active than Au, and that step and edge sites lead to a further increase in the reaction rate.

If support effects do not influence activity, the above results suggest that supported Cu particles should yield activities higher than supported Au. The authors, however, cite numerous experimental results demonstrating that Au supported on ceria achieves higher conversions and faster reaction rates than the analogous Cu/ceria catalysts. The authors' experimental reaction rates and computed activation barriers demonstrate the low activity of Au compared to Cu, and suggest that high activity of Au/ceria must be the result of support interactions that activate the otherwise inactive Au clusters. Conversely, DFT results predicting low activity over unsupported Au are in qualitative agreement with the experimentally determined activity of Au supported on ZnO, which suggests that ZnO does not activate the particle or participate in the reaction mechanism. Liu, Rodriguez, and coworkers[115] also computed the activity of charged Cu and Au particles to determine whether charge transfer between the cluster and the support could alone alter the activity of the metal clusters. The DFT computed activation barriers over such ionic clusters show that neither cationic nor anionic Au particles are as active as Cu particles, demonstrating that

the activity of Au/ceria is not solely the result of active sites on ceria-stabilized ionic Au species. Since the metal sites alone cannot activate the gas-phase reactants, the reaction may proceed through interfacial sites involving both the metal cluster and oxide support. The support not only activates the metal clusters, but likely plays a role in the reaction mechanism. The authors contrast this observation with the behavior of ZnO supported catalysts, in which the oxide may merely act as an inert substrate supporting the Au cluster for this reaction. These results demonstrate the utility of DFT (applied together with experimental studies) for differentiating between *active* and *spectator* supports.

4.3.1.3 Characteristics of Au Supported on CeO_2

DFT methods can model both the structural and the electronic properties of a metal–oxide system. Since the computational expense of DFT scales heavily with system size, it is often necessary to analyze small model systems that, hopefully, capture the fundamental behavior at play in larger systems. This strategy was employed by Liu and coworkers, who conducted systematic DFT calculations investigating the binding trends and electronic properties of a *single* Au atom adsorbed on stoichiometric $CeO_2(111)$, on $CeO_2(111)$ with O-vacancies, and on reduced $Ce_2O_3(0001)$ surfaces.[71] Many properties observed for the single Au atom can be extended to make predictions regarding the properties of larger clusters. Au atoms bind most strongly to O-vacant sites on the partially reduced CeO_2 surface ($\Delta E_{bind} = -1.86$ eV), and they bind least strongly to the fully reduced Ce_2O_3 surface ($\Delta E_{bind} = -0.86$ eV). Binding affinity on the stoichiometric CeO_2 is also considerable in magnitude, with $\Delta E_{bind} = -1.26$ eV. Using a Bader charge analysis,[122] the authors demonstrated that Au adsorbed in an oxygen vacancy on reduced CeO_2 has a negative partial charge (-0.58 e), while Au adsorbed on stoichiometric CeO_2 has a positive partial charge ($+0.35$ e). The negative partial charge on Au adsorbed in an O-vacancy suggests that Au acts as a reduction center, accepting a portion of the two electrons left in the surface after the formation of an O-vacancy. This demonstrates that oxygen vacancies serve as anchor sites that accommodate negative $Au^{\delta-}$ species adsorbed on the ceria surface.

However, the authors note that CO binding energy calculations demonstrate that positive Au species, rather than negative species, are capable of adsorbing CO, and that these sites may play a key role in the WGS reaction mechanism. A density of state (DOS) analysis can determine how ceria stabilizes an active $Au^{\delta+}$ species within $Au_{n>1}$ clusters. The authors posit that the empty band of cerium *f*-orbitals near the Fermi level accepts a Au $6s^1$ electron that would otherwise enter an anti-bonding $Au(6s)O(2p)$ orbital. A single Au atom can serve as a reduction center, stabilizing an O-vacancy in the ceria lattice. In turn, cerium atoms can subsequently oxidize adsorbed Au atoms by accepting a Au-$6s^1$ electron in the *f*-band. This explains the WGS activity of Au supported on *reduced* CeO_2: the O-vacancy serves as an anchor site for an Au atom, which then serves as a nucleation base for subsequent Au atoms that are oxidized by the surrounding Ce neighbors. This creates $Au^{\delta+}$ sites that favorably adsorb

gas-phase reactants, which can then interact with neighboring sites on both the cluster and the oxide. This result offers guidance for determining the behavior of larger Au clusters on the ceria surface, and how these structures may create active sites for the WGS mechanism. This study demonstrates the value of DFT for analyzing the confluence of electronic and structural particle–support interactions that affect reaction mechanisms.

4.3.1.4   *WGS Mechanism over Au Supported on CeO$_2$*

Next we consider studies that use DFT explicitly to evaluate the energetics of candidate reaction mechanisms over various Au/ceria surface configurations. Chen *et al.*[26,123] used DFT + U to probe possible reaction mechanisms that proceed over the Au/ceria interface. In one study they examined redox and formate mechanisms over Au$_3$ and Au$_{10}$ clusters on CeO$_2$(111).[123] Both mechanisms feature rate limiting water O–H bond dissociation steps occurring over CeO$_2$ O–vacancies. The redox mechanism requires H$_2$O to dissociate after filling an oxygen-vacancy on the ceria surface, leaving H$_2$ on the metal cluster after oxidizing the support. The CO reactant, which is adsorbed on the metal cluster, then reduces the oxide by removing an O atom from the ceria lattice, thus recreating an O-vacancy. Similarly, the formate mechanism requires an O–H bond breaking step after H$_2$O adsorbs in an O-vacancy. CO adsorbed on the metal cluster then removes an H atom from the OH group adsorbed in an oxygen-vacancy, creating a CHO group on the cluster. The resultant CHO group then removes an O from the oxide surface and desorbs as CO$_2$, with an H atom left behind on the metal cluster. This recreates the O-vacancy in the surface, and leaves an H atom that can react with H$_2$O in the next cycle, thus desorbing H$_2$ and leaving OH adsorbed in the O-vacancy. The authors consider that breaking OH bonds to refill O-vacancies is rate limiting in both cases. DFT is used to determine the activation barriers for possible elementary steps that accomplish the necessary O-vacancy filling step. The authors conclude that both mechanisms must overcome a reaction barrier greater than 1 eV, which is prohibitive at low temperatures. This suggests that neither mechanism can explain the experimentally observed activity of Au/ceria toward WGS at low temperatures, and for this reason they propose a different mechanism, the carboxyl mechanism, that is unique to the supported system and not subject to this limitation.

In a second study,[26] Chen *et al.* propose a carboxyl mechanism for WGS over Au/ceria in which the rate-limiting H$_2$O dissociation step occurs at the Au/ceria interface. The mechanism, summarized in the reaction energy diagram shown in Figure 4.3, requires H$_2$O from the gas phase to fill an oxygen vacancy near an Au cluster. Once in the vacancy, the H$_2$O molecule dissociates, as shown in Figure 4.4, by allowing H to adsorb on the metal cluster while leaving OH behind on the oxide. The OH group then reacts across the Au/ceria interface with CO adsorbed on the metal cluster, thus forming a carboxyl group and regenerating the oxygen vacancy in the ceria lattice. To support the carboxyl mechanism further, the authors use a microkinetic model to compare the performance of the carboxyl mechanism to the formate and redox mechanisms
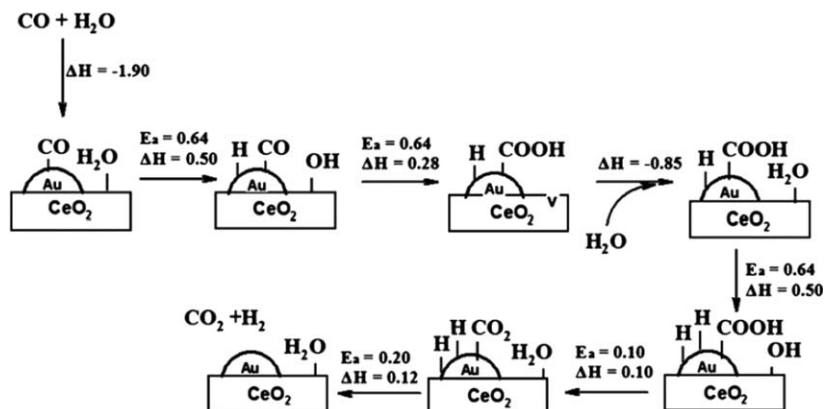
Figure 4.3   Water–gas-shift reaction mechanism proceeding through a carboxyl sur-
face intermediate as proposed by Chen *et al.*
(Reprinted with permission from ref. 26 Copyright 2011 Royal Society of
Chemistry)
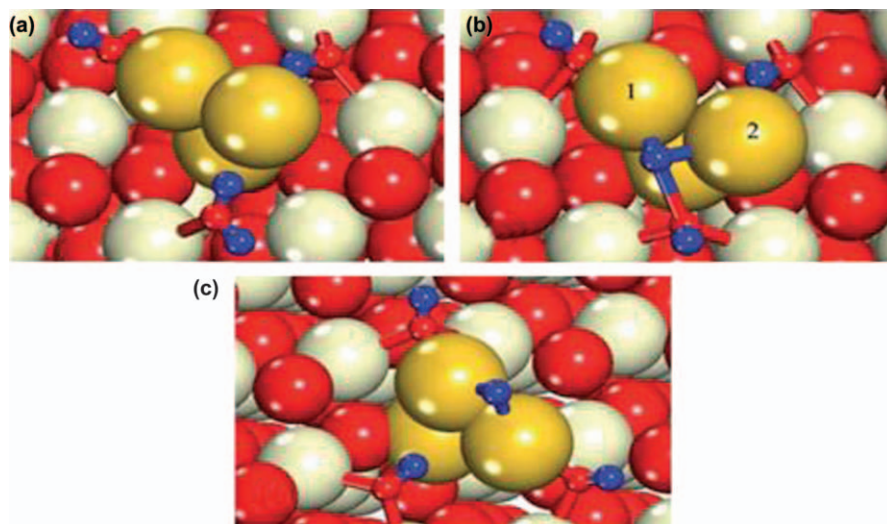
Figure 4.4   (a) Initial, (b) transition, and (c) final structures for the dissociation of
H_2O across the $Au–CeO_2$ interface, where H = blue, Au = yellow, O = red,
Ce = white.
(Reprinted with permission from ref. 26 Copyright 2011 Royal Society of
Chemistry)

discussed earlier. The result shows that the carboxyl mechanism yields a higher
rate than the formate and redox mechanisms, and therefore better explains the
high activity of Au/ceria catalysts. The carboxyl mechanism requires sites at
the Au–ceria boundary, thus demonstrating the importance of considering

metal–support interactions when postulating reaction mechanisms on supported metal–oxide catalysts.

4.3.2   *Ab Initio* Thermodynamics

The studies discussed in the previous sections did not explicitly consider the effects of a gas-phase environment at operating temperatures and pressures. Although providing useful insight, the methods employed could not model thermodynamic stabilities, adsorbate coverage effects, or *free energy* differences. This section will review studies that apply *ab initio* thermodynamics to accomplish such assessments. We first review the work of Reuter and Scheffler on RuO_2 systems, which was one of the first applications of *ab initio* thermodynamics to catalysis. This study assessed the catalytic behavior of an oxide, which is readily extended to studies of supported metal–oxide catalysts because the oxide support often plays an active role in the catalytic mechanism. We then will consider examples that apply *ab initio* thermodynamics to supported metal–oxide catalysts. In particular, we highlight systems in which particle–support interactions play an important role in overall catalytic activity.

4.3.2.1   *Investigating Oxide Supports*

4.3.2.1.1   Background.   When conducting DFT to assess catalytic mechanisms over a surface, it is essential to choose an appropriate model. That is, one must choose a model surface that is thermodynamically or kinetically stable under the reaction conditions of interest. Reuter and Scheffler applied the formalism of *ab initio* thermodynamics in a series of studies that assess the structure, stability, and reactivity of the $RuO_2(110)$ surface in equilibrium with a mixed O_2 and CO atmosphere.[100,102] This series of publications was one of the earliest applications of *ab initio* thermodynamics, and effectively demonstrates the methodology for bridging the gap between DFT calculations (at zero T and P) and experimental results under catalytic reaction conditions. They applied *ab initio* thermodynamics to determine the relative stability of $RuO_2(110)$ surface terminations in different oxidation states as a function of T, P_{O_2}, and P_{CO}. Although these studies were explicitly applied to the catalytic properties of RuO_2 toward CO oxidation, the formalism presented therein can be readily extended to studies investigating the stability and activity of oxide surfaces in supported metal–oxide systems. This methodology can be used to determine plausible surface models for detailed analyses of the reaction mechanism energetics.

4.3.2.1.2   Stability of RuO_2 Surface Phases.   Reuter and Scheffler first outline the theory and methodology of *ab initio* thermodynamics in a study applied to RuO_2 in equilibrium with an O_2 atmosphere.[100] The authors consider three possible surface terminations of $RuO_2(110)$. The $RuO_2(110)$–O_{bridge} surface is predicted to be the most stable because it has the lowest number of uncoordinated O atoms and has no net dipole. The second

surface considered is $RuO_2(110)$–O_{cus}, which features coordinately unsaturated (cus) oxygen atoms placed directly above the surface row of Ru atoms, creating a 6-fold coordination on all surface Ru atoms. The final structure, $RuO_2(110)$–Ru, has rows of 5-fold coordinated cus-Ru atoms and 4-fold coordinated bridge-Ru atoms on the oxide surface. The authors investigate the stability of the three $RuO_2(110)$ surface terminations by calculating the surface free energy of each termination as a function T and P_{O_2}. These calculations show that at typical operating temperatures for CO oxidation ($T = 600$ K), the O-bridge surface termination is most stable at lower P_{O_2} and that the over oxidized O-cus surface is favored at high P_{O_2}. The Ru terminated surface is never favored in the P_{O_2} ranges of interest. The results reveal that the RuO_2–O_{bridge} surface termination is not always the most stable, and that a different surface phase is likely to form at high P_{O_2}. The authors argue that the emergence of the RuO_2–O_{cus} phase at high O_2 chemical potentials, which was previously unknown, must be considered when interpreting experimental data collected under such conditions. This result highlights the importance of investigating the stability of a system for the entire temperature and pressure ranges of interest before drawing conclusions regarding the nature of active surface sites.

In subsequent studies, the authors incorporated the effect of both P_{O_2} and P_{CO} on surface site occupation.[101] Using the resultant surface phase diagram they predict the regions in T,P space that are likely to display the highest catalytic activity. They conclude that the boundary between the O_{br}/CO_{cus} phase and the O_{br}/O_{cus} phase will balance CO_2 desorption, creating O-vacancies at O_{cus} sites with the subsequent filling of O_{cus} vacancies by gas-phase oxygen. Deep in the O_{br}/O_{cus} phase region, catalytic activity will be hampered by the high O_{cus} vacancy formation energy; whereas, in the CO_{br}/O_{cus} phase, CO_{br} will consume O_{cus} faster than the resultant vacancies can be refilled by the gas phase. These results demonstrate the important role phase coexistence plays in catalytic mechanisms, and they exemplify the utility of *ab initio* thermodynamics for identifying favored reaction paths in T, P regions, bridging the gap between quantum calculations and experimental conditions.

4.3.2.2 Investigating Metal Clusters on Oxide Supports

4.3.2.2.1 Background. The formalism presented in the previous section for predicting the stability of oxide surfaces in equilibrium with a multi-component gas phase is readily extended to systems that contain catalytic metal particles supported on oxide surfaces. Identifying stable particle–support constructions is indispensable for predicting the catalytic activity of the particle–support interface. This section will outline studies on reducible oxides (TiO_2 and CeO_2) that display unique particle–support interactions where the oxide support plays an active role in the catalytic mechanism. These examples demonstrate the ability of *ab initio* thermodynamics to determine the stability of metal clusters on oxide supports under realistic catalytic conditions. Such calculations can be used in concert with DFT reactivity studies

to assess the activity of stable metal–oxide surfaces. Together, these methods offer a powerful means for predicting and characterizing the catalytic activity of a wide range of metal–oxide systems.

4.3.2.2.2 Au/TiO$_2$. In a study by Laursen and Linic,[68] the authors analyzed the behavior of Au on titanium oxide. They considered two model Au formations on the oxide surface: a nanorod and a 2 mono-layer sheet. They assessed the stability of these formations as a function of oxygen pressure over reduced, stoichiometric, and oxidized surfaces. The results shown in Figure 4.5(c) demonstrate that both the nanorod and sheet constructions are most stable over the oxidized support. Formations over the reduced support can be stabilized at high temperatures in a highly reducing atmosphere at low oxygen chemical potential.

After determining the stability of these model systems, the authors calculated the adsorption and dissociation energies of O$_2$, along with the adsorption energy of CO, to probe the activity of possible sites on the supported Au clusters. The results of these calculations, shown in Figure 4.5(a), show that the adsorption energy for both O$_2$ and CO is significantly more exothermic over both the reduced and oxidized catalysts compared to equivalent sites on Au formations supported by a stoichiometric titania surface. The same trend holds for the dissociation barrier of O$_2$ over all three catalyst models shown in Figure 4.5(b). The authors note that the most favorable adsorption sites involve Au atoms that are adjacent to Au atoms bound to point defects on the reduced and oxidized surfaces (the defects consist of an O-vacancy or an added O-atom, respectively). They explain this trend in terms of bond conservation theory, in which the strengthening of an Au–defect bond will weaken the neighboring Au–Au bond to the next adjacent Au atom, thus creating a chemically active site on the adjacent Au atom for bonding with a gas-phase molecule. The authors support this theory with charge density and local density of states (LDOS) calculations, which show that charge transfer between the surface and the particle (either from Au to the surface for oxidized-TiO$_2$ or *vice versa* for reduced-TiO$_2$) results in a strong polar–covalent bond between the Au atom and the point defect. This in turn weakens the bond to the next adjacent Au atom, making adsorption on that atom more favorable. The strong covalent bonds present in both the reduced and oxidized systems are largely absent in the stoichiometric system. Both unsupported Au nanorods and nanorods supported on the stoichiometric surface display low activity because neither system is activated by the covalent-type Au–oxide bonds present in the defected systems. The authors conclude that point defects on the oxide surface not only serve as anchor points for the metal clusters, but that they are also largely responsible for activating the particle through charge transfer. This contrasts with the findings of Corma and coworkers, who found that *neutral* Au particles display higher activity toward the dissociation of H$_2$, demonstrating the need to assess the relative activity of both charged and neutral clusters.[56,57] These studies exemplify the importance of particle–support interactions for predicting the catalytic activity of a system, and demonstrate how *ab initio*
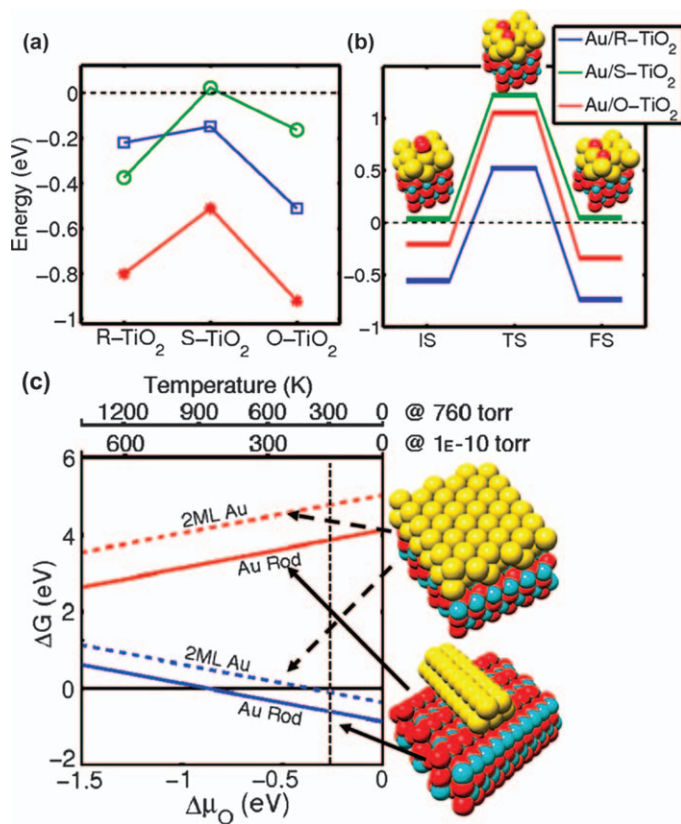
Figure 4.5 (a) Adsorption energy of molecular oxygen and CO with respect to gas-phase species on reduced, stoichiometric, and oxidized Au/TiO_2 surfaces for oxygen on a Au sheet (green, o), oxygen on a Au nanorod (blue, □), and CO on a Au sheet (red, *). (b) Activation barrier for O_2 dissociation over an Au bilayer sheet on reduced, stoichiometric, and oxidized TiO_2. (c) Free energy calculated as a function of oxygen chemical potential for Au rod and bilayer sheet structures on reduced (red, positive slope) and oxidized (blue, negative slope) TiO_2.
(Reprinted with permission from ref. 68 Copyright 2009 American Chemical Society)

thermodynamics – in conjunction with standard DFT energy calculations – can explain the stability and activity of oxide-supported metal clusters.

4.3.2.2.3 Pt/TiO$_2$. In a similar study, Ammal and Heyden[124,125] investigated the effects of particle–support interactions between Pt and TiO_2 under water–gas-shift T,P conditions. They first determined the effect of Pt clusters on the reducibility of titania by systematically assessing the stability of small Pt_n ($n = 1$–8) clusters adsorbed on a partially reduced $TiO_2(110)$ surface. Using *ab initio* thermodynamics, the authors calculated the free energy

change for forming a single oxygen vacancy in the TiO_2 surface under oxidizing (O_2-rich) and reducing (CO-rich or H_2-rich) atmospheres. Not surprisingly, the authors found that vacancy formation is never favorable under oxidizing conditions. However, they found that Pt clusters greatly increase the favorability of oxygen vacancy formation under CO- and H_2-rich atmospheres. This is demonstrated by the results reproduced in Figure 4.6(a)
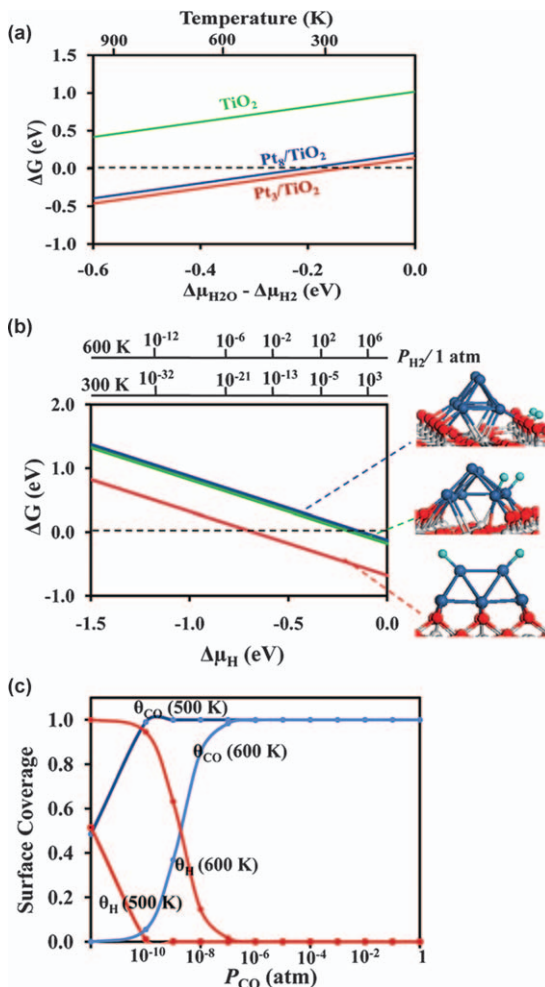
Figure 4.6 (a) Free energy difference for oxygen vacancy formation on the clean TiO_2 surface (green, top), on TiO_2 in the presence of Pt_8 (blue, middle), and in the presence of Pt_3 (red, bottom). (b) Free energy of H_2 adsorption on the oxide (blue, top), the metal–oxide interface (green, middle), and on the metal cluster (red, bottom). (c) Computed equilibrium surface coverage of CO and hydrogen at constant $P_{H2} = 1$ atm.
(Reprinted with permission from refs. 125,126 Copyright 2011 American Chemical Society)

showing vacancy formation free energy as a function of P_{H_2} and T. Vacancy formation energy is significantly lower for surfaces with Pt_n clusters compared with the clean TiO_2 surface, which never favors oxygen vacancy formation in the T,P regions of interest. These results are similar to those of Laursen and Linic discussed above, in which the metal particle is anchored to the reduced TiO_2 surface through a covalent-type interaction that is largely absent over the stoichiometric surface. The subsequent charge transfer from the reduced TiO_2 surface to the Pt particle alters the adsorption behavior of gas phase molecules on the Pt cluster. This further demonstrates the unique effects of particle–surface interactions.

The authors next assessed the stability of H_2 and CO gas phase adsorbates on the Pt_8 cluster, at the Pt–TiO_2 interface, and on the TiO_2 surface adjacent to the Pt cluster. They computed the free energy of adsorption for gas-phase molecules at these sites, as well as calculating the equilibrium surface coverage as a function of partial pressure and temperature. It is possible that the WGS reaction mechanism involves hydrogen spillover from the metal particle to the TiO_2 surface. For this reason, the authors investigated H_2 adsorption in the vicinity of a Pt cluster, which is summarized in Figure 4.6(b). The presence of H atoms at the Pt–TiO_2 interface can have adverse effects on the catalytic performance of the surface if H atoms bind too strongly to the interfacial sites under WGS conditions. The results shown in Figure 4.6(b–c) show that H atoms bind more strongly to Pt cluster sites than to interfacial Pt and O sites, suggesting that interfacial sites will not hinder hydrogen spillover between the Pt cluster and the oxide surface. By calculating the surface coverage of CO and H at various temperatures, the authors also show that CO adsorption on Pt cluster sites will dominate over H adsorption, indicating that Pt cluster sites will be filled by adsorbed CO under WGS conditions. These results demonstrate that interfacial sites will remain open under WGS conditions, and that they may be responsible for the high WGS activity of the catalyst. The authors note that this result corroborates experimental findings,[126,127] in which the WGS reaction rate scales positively with the interfacial boundary length. Using *ab initio* thermodynamics, the authors were able to assess the stability of candidate model systems for the Pt/TiO_2 surface under WGS conditions. Having identified a plausible model system, the authors mention their plans to use DFT to investigate the WGS mechanism over the Pt/TiO_2 interfacial model they identified in this study. We note that the authors also conducted a similar study on an analogous Pt/CeO_2(111) system,[128] which applies similar methods to characterize the effect of Pt–ceria interactions.

4.3.2.2.4 Cu/CeO$_2$. The previous studies have shown that metal clusters typically enhance the reducibility of metal–oxide surfaces, thus altering the electronic properties of both the metal cluster and the oxide surface. Fabris and coworkers[73] demonstrate that this trend does not hold for all metal–oxide supported systems. They conducted a systematic computational study of Cu/CeO_2 systems that feature Cu atoms adsorbed on a stoichiometric surface, on a surface containing oxygen-vacancies, and on a surface containing

cerium-vacancies. In particular, they use *ab initio* thermodynamics to assess the stability of Cu adsorption on the various CeO_2 surfaces in equilibrium with an oxygen atmosphere. *Ab initio* thermodynamics predicts that Cu typically prefers to adsorb on the stoichiometric CeO_2 surface, rather than on surfaces containing oxygen-vacancies or cerium-vacancies. These results are shown in Figure 4.7, where the free energy of adsorption is plotted against oxygen chemical potential. Under oxidizing conditions, the formation of surface solution phases featuring a Cu atom substituted for a Ce atom is thermodynamically favored over Cu adsorption on the stoichiometric surface.

These observations lead to interesting conclusions regarding the redox behavior of Cu/CeO_2. The authors note that substituted Cu ions form stabilized CuO_4 units that permit the reversible release of oxygen under catalytically relevant thermodynamic conditions. This is reflected by the stability of the $O^{vac}/Cu@Ce^{vac}$ phase that neighbors the $Cu@Ce^{vac}$ phase seen in Figure 4.7. This demonstrates that the surface can act as an oxygen buffer during reactions conducted under oxidizing conditions. Furthermore, it shows that redox processes over Cu/CeO_2 surfaces do not involve the reduction of cerium atoms (from Ce^{4+} to Ce^{3+}) neighboring oxygen-vacancies, which is typically characteristic of reaction paths involving a CeO_2 redox process. Other metal–ceria systems (*e.g.* Au/ceria, discussed in previous sections) typically feature a redox mechanism in which metal clusters adsorbed on the surface stabilize the
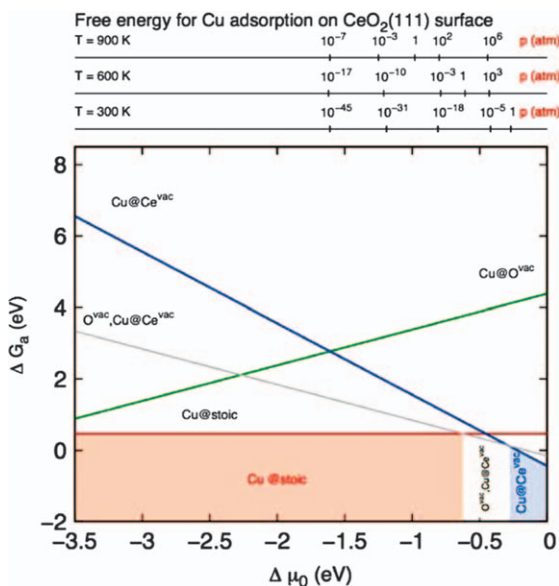
Figure 4.7   Free energy for the adsorption of Cu adatoms on stoichiometric ceria (red), on ceria with an oxygen vacancy (green), on ceria with a cerium vacancy (blue), and on ceria with both an oxygen and a cerium vacancy (gray). (Reprinted with permission from ref. 73 Copyright 2010 American Institute of Physics)

formation of oxygen vacancies. In the case of copper, however, oxygen vacancies are stabilized by substitution defects where Cu atoms fill Ce vacancies. *Ab initio* thermodynamics enabled the authors to determine Cu/CeO_2 structures that are thermodynamically favored under reactive conditions. Together with electronic structure calculations, the authors demonstrate that the redox behavior of Cu/CeO_2 does not follow the typical redox mechanism of other metal/ceria surfaces.

4.3.3 Classical Atomistic Modeling

The computational expense of quantum (QM) methods limits these methods to highly idealized system models, such as the single crystal surfaces and small ($\sim M_{n<8}$) clusters considered in the studies above. However, many catalytically interesting properties of supported metal–oxide systems arise from structural irregularities and possibly from the dynamic effect of surface reconstruction during reaction. Although it is difficult to characterize such effects using QM, it becomes possible with the use of empirical force-fields that have a relatively low computational expense. Reactive force-fields are designed to model bond dissociation and formation, and can therefore be implemented in *reactive* molecular dynamics (RMD) simulations that are capable of describing the dynamic nature of a catalyst at longer length and time scales (up to $\sim 10^4$ atoms and ~ 1 ns). This section will review research examples implementing the ReaxFF potential to model dynamic catalyst behavior under reactive conditions. The work described herein demonstrates that reactive force-field methods can be readily extended to model supported metal–oxide catalysts.

4.3.3.1 The ReaxFF Force Field

4.3.3.1.1 Background. ReaxFF uses bond-length/bond-order relationships to model bond formation and dissociation in covalent systems, making it readily applicable to catalytic systems. This section will summarize two studies that demonstrate the ability of ReaxFF to describe supported metal–oxide catalysts accurately. The first study focuses on the catalytic properties of nickel surfaces and particles interacting with hydrocarbon reactants. The second study demonstrates the use of ReaxFF to describe complicated multi-metal–oxide (Mo/V/O) catalysts under reactive hydrocarbon environments. Together these studies show how ReaxFF extends the reach of computational methods to length and time scales required for characterizing the dynamic behavior of supported metal–oxide catalysts.

4.3.3.1.2 Hydrocarbon Catalysis on Metals. The ReaxFF force-field can model catalytic properties of metal clusters toward C–H and C–C bond activation. This is exemplified by the work of Mueller, van Duin, and Goddard, in which the authors developed a Ni/C/H potential by parameterizing the ReaxFF force-field to reproduce a training set populated with DFT results for hydrocarbon–nickel adsorption energies, activation barriers, and bulk

formation energies.[129] The authors note that surface defects may play an important role in reaction paths that lead to the high activity of the nickel surface, and that surface science experiments of hydrocarbon chemisorption and decomposition often seek to limit the number of defects on the surface in order to characterize the reactivity of ordered low-index nickel surfaces. Similarly, DFT is computationally unable to reach the necessary system sizes for analyzing the effect of defects on irregular surfaces. For these reasons, the authors applied the Ni/C/H force-field in reactive molecular dynamics (RMD) simulations to assess the reactivity of various hydrocarbons over Ni catalyst particles that expose multiple irregular surface terminations, yielding insight into the role defect sites play in Ni-catalyzed hydrocarbon reaction mechanisms.[130]

The study consisted of a series of RMD simulations with a spherical Ni particle consisting of 468 atoms surrounded by a single-species hydrocarbon gas phase in an $80\times80\times80$ Å^3 periodic box. Simulations were conducted with six representative hydrocarbon species (methane, ethyne, ethene, benzene, cyclohexane, and propene) that were chosen to cover a variety of hydrocarbon behaviors arising from varying degrees of saturation. In each simulation, the temperature was ramped from 500 K to 2500 K at a rate of 20 K ps^{-1} over the course of the 100 ps simulation. The authors extracted species population data at each time step, thus identifying reaction intermediates and their corresponding formation and decomposition rates. These data were then used to construct reaction networks from which elementary reaction paths can be identified. The results and analysis of the simulation for propene are reproduced in Figure 4.8. The figure depicts the initial and final structures of the system, as well as the molecular population analysis as the simulation progresses. As seen in the figure, the authors can determine the temperatures at which key reactive events occur. This includes the temperatures at which gas-phase propene begins to chemisorb on the surface (T_A), that at which dehydrogenation commences (T_H), and that at which carbon–carbon bonds are broken (T_C). These temperatures yield insight into the kinetic barriers for hydrocarbon dissociation over nickel particles.

Analysis of the simulation trajectory yields reaction networks that reveal the preferred reaction mechanism over the Ni catalyst. For propene, molecules begin to chemisorb rapidly because C–C π bonds can be readily broken to form C–Ni σ bonds. Correspondingly, chemisorption of saturated hydrocarbons does not occur until higher temperatures, where C–H bonds are broken by dehydrogenation. Analyses of the simulation trajectories show that C–H bond breaking is catalyzed by the insertion of a Ni atom within the C–H bond. The simulations also reveal that dehydrogenation typically precedes C–C bond scission, which is reflected in the figure by a low T_H compared to T_C. In contrast with DFT approaches, reaction paths are identified by MD analysis as opposed to being hypothesized and evaluated explicitly, which allows the method to find reaction paths that are not immediately apparent. These results have many implications for designing Ni catalysts for hydrocarbon treatment. This work exemplifies the ability of empirical force-fields to characterize reactions
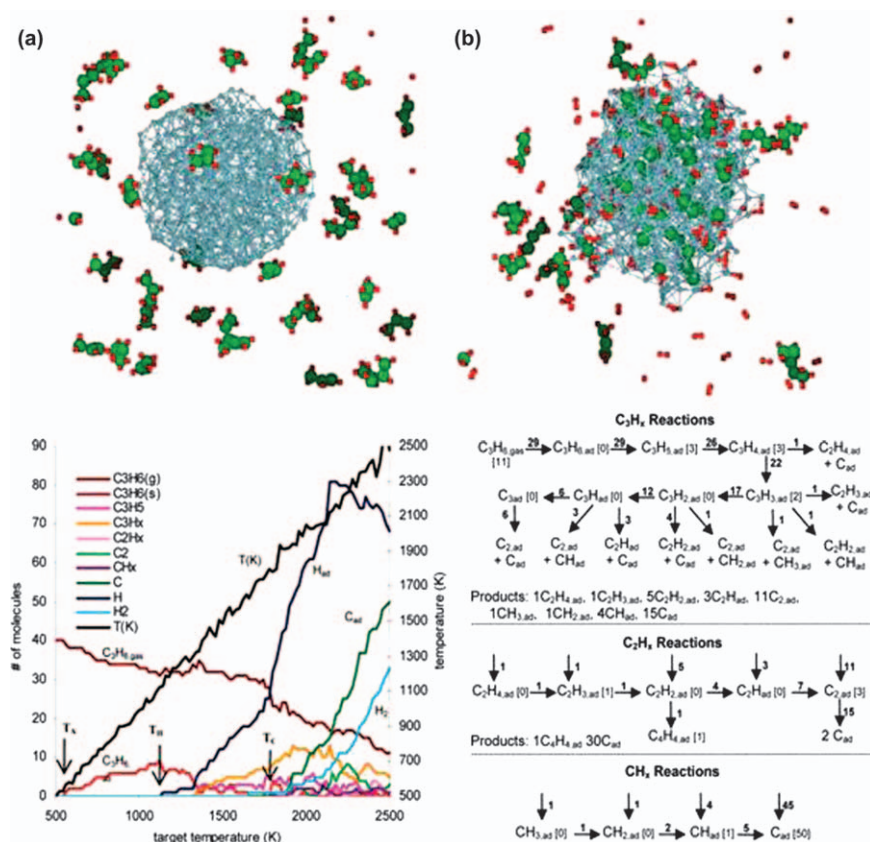
Figure 4.8 (top) Initial and final structures of a RMD simulation demonstrating propene adsorption and decomposition on a nickel nanoparticle. (bottom) Molecular populations plotted against simulation temperature, and the corresponding reaction networks. Numbers in brackets indicate the number of species present at the end of the simulation and numbers over arrows indicate the corresponding number of reactive events.
(Adapted with permission from ref. 131 Copyright 2010 American Chemical Society)

involving covalent hydrocarbon species interacting with irregular metal surfaces, which is necessary for modeling supported metal–oxide heterogeneous catalysts at large scales.

4.3.3.1.3 Multi-metal–Oxide Catalysis. The ReaxFF potential has also been utilized to study the catalytic properties of complex metal oxides. Chenoweth *et al.* developed and implemented a V/O/C/H force-field that, when combined with the existing hydrocarbon force-field, can model the interaction between gas-phase hydrocarbons and the vanadium oxide surface.[131,132] For motivation, the authors cite numerous examples in which V_2O_5 is used to catalyze industrial processes that selectively oxidize both

saturated and unsaturated hydrocarbon species, such as the conversion of methanol to formaldehyde. They stress that, although V_2O_5 can be used for the oxidative dehydrogenation of methanol, it lacks selectivity when applied to the partial oxidation of larger hydrocarbons. The selectivity of vanadium oxide can be improved with the addition of appropriate supports and metal dopants (such as V, Te, Ta, and Nb) that alter the surface geometry and electronic structure. The addition of supports and dopants to form multi-metal–oxide catalysts often introduces a confluence of structural and electronic effects that are too complex for experimental efforts to untangle. For this reason, the authors propose that theoretical methodologies, such as RMD simulations *via* ReaxFF, are essential for establishing the necessary atomistic understanding of reaction processes over the complex oxide surface for designing more selective catalysts.

To demonstrate the validity of the ReaxFF potential for modeling catalytic V/O/C/H interactions, the authors simulated the oxidative dehydrogenation of methanol over the $V_2O_5(001)$ surface.[131] They conducted a 250 ps NVT-MD simulation of a three-layer oxide slab surrounded by 30 gas-phase methanol molecules in a $20\times20\times20$ Å^3 periodic box. A dual temperature constraint was applied in which the oxide slab was held at 650 K and the gas-phase molecules were held at 2000 K. The final MD structure, along with the species population analysis, is shown in Figure 4.9. Methanol species adsorb on the oxide surface and, after rearrangement, desorb as formaldehyde. Analysis of molecular populations and the MD trajectory shows that the reaction mechanism proceeds through the abstraction of hydrogen from the methyl group. The authors note that this result seems to contradict experimental evidence (from DRIFTS spectroscopy) that suggests an O–H bond dissociation mechanism. The authors demonstrate, however, that the C–H abstraction path is preferred on the fully
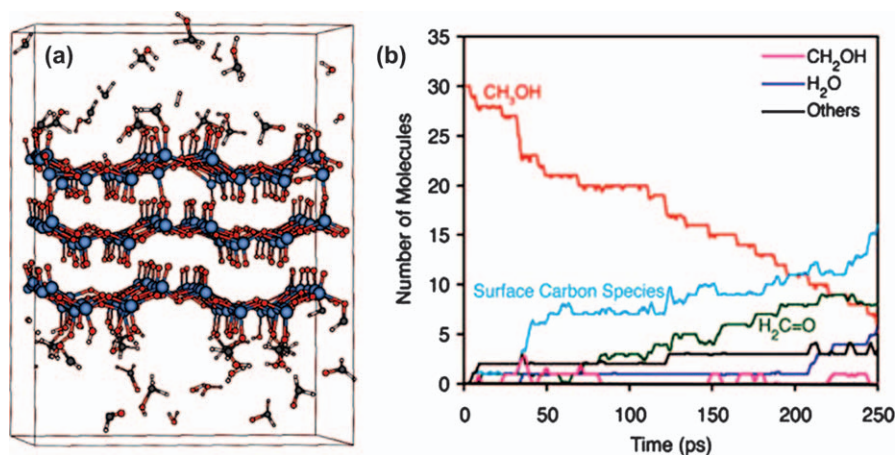
Figure 4.9   (a) Final structure of a NVT–MD simulation of methanol interacting with a V_2O_5 slab and (b) the corresponding species population plot. (Reprinted from ref. 132 Copyright 2008 American Chemical Society)

oxidized V_2O_5(001) surface and that the O–H abstraction path is preferred over a defect site where an oxo- group has been removed from the surface. This result demonstrates the viability of the ReaxFF method for oxide-based catalysis, as well as exhibiting the power of atomistic modeling for complementing experimental efforts to discern structural factors that influence the reaction path.

The ReaxFF method can also be used to determine the structure and nature of active sites on complex oxide surfaces. This is demonstrated by the same authors in a subsequent publication,[132] in which they applied ReaxFF to predict the structure of a highly disordered multi-metal Mo_3VO_x catalyst. As mentioned earlier, the selectivity of vanadium oxide catalysts toward the partial oxidation of hydrocarbons can be altered by the addition of metal dopants to form multi-metal–oxides (MMO). MMO catalysts typically feature partial or mixed occupations of crystallographic sites, making it difficult to characterize the structure and nature of active sites by experimental methods. The authors applied the ReaxFF potential to conduct a combined Monte Carlo/reactive dynamics (MC/RD) procedure to determine the Mo_3VO_x structure. The catalyst surface has metal sites that can be occupied by either Mo or V atoms. The MC/RD scheme identifies the preferred occupation of each site by systematically interchanging two atoms that occupy the same crystallographic site and determining the resultant energy change after re-optimizing the structure through RD. The new structure is either accepted or rejected according to the MC-Metropolis criterion,[133] and the process is repeated until the energy converges at an optimal configuration for the chemical environment of the system.

The authors used the optimized structure to conduct RMD simulations in which hydrocarbons interact with the catalyst. The optimized catalyst displays several channels in the oxide through which hydrocarbons can diffuse to reach active sites. This particular simulation reveals that propane can diffuse through the $C7_2$-labeled channel in the oxide, but not through the $C7_1$-labeled channel. Such observations can reveal structural factors that influence catalyst selectivity, because different hydrocarbon species will tend to diffuse through different channels. This property can be exploited to design highly selective MMO catalysts. This result demonstrates the applicability of the ReaxFF method for characterizing complex metal–oxide catalysts, which can be readily extended to supported metal-cluster/metal-oxide catalysis.

4.3.4 Combined Application: Hydrocarbon Activation over Pd/CeO$_2$

In the previous sections, we discussed separate applications of DFT, *ab initio* thermodynamics, and empirical force-fields to demonstrate the capabilities and limitations of each computational method applied to supported metal–oxide catalysis. As mentioned earlier, these methods can be applied together to achieve a broader understanding of the factors affecting catalytic activity, scaling from electronic structure to large-scale surface rearrangement and adsorbate coverage effects. This section highlights an ongoing multi-scale study conducted across our laboratory combining these methods in an effort to

identify factors contributing to high activity of Pd/ceria catalysts toward hydrocarbon conversion.

4.3.4.1 Background

Palladium supported on ceria is an effective catalyst for hydrocarbon oxidation and is a promising candidate for application in solid-oxide fuel cell (SOFC) anodes,[48–50] automotive three-way catalysis,[43,46] catalytic combustion,[3,12,87] and water–gas-shift catalysis.[31,134] There is, however, little consensus in the literature regarding the chemical and structural properties of the active sites and reaction mechanisms on the Pd/ceria surface. Under reaction conditions, multiple Pd/ceria surface morphologies are possible, each with unique catalytic activity. Examples of such morphologies include the following: metallic Pd clusters adsorbed on the ceria support, oxidized palladium in PdO surface phases, and palladium incorporated in cerium lattice vacancies as a solid–solution $Pd_xCe_{1-x}O_y$ phase. Experimental evidence suggests that strong electronic interactions between Pd and ceria stabilize oxidized Pd species that in turn are capable of activating C–H bonds in hydrocarbons. This is evident in the work of Colussi *et al.*,[87] which uses high-resolution transmission electron spectroscopy (HRTEM) and DFT to show that Pd/ceria catalysts prepared by solution combustion synthesis (SCS) contain a Pd^{2+}/CeO_x solid solution that is absent in Pd/ceria catalysts prepared by traditional incipient wetness impregnation (IWI). The Pd^{2+}/CeO_x phase forms when Pd atoms are systematically substituted for Ce atoms in the ceria lattice, thus forming a square planar geometry characteristic of Pd^{2+} in bulk PdO. Pd/ceria samples prepared by SCS achieved considerably higher methane combustion rates compared to the analogous catalysts prepared by IWI, suggesting that the presence of Pd^{2+}/CeO_x plays an important role in hydrocarbon activation. Similar results for the combustion of propane and dimethyl ether over Pd/ceria prepared by SCS further emphasize the importance of oxidized $Pd^{\delta+}$ species, while also suggesting the importance of metallic Pd^0 clusters coexisting on the surface with the Pd^{2+}/CeO_x phase.[4] In a similar study, Misch *et al.* used X-ray diffraction (XRD) and X-ray photoelectron spectroscopy (XPS) to characterize $Ce_{1-x}Pd_xO_\delta$ catalysts before and after the catalytic oxidation of methane.[88] Interestingly, their results suggest that metallic Pd^0/CeO_2, rather than an oxidized $Pd^{\delta+}$ species, is essential for high catalytic activity. Furthermore, a recent study by Gorte and coworkers[12] has synthesized Pd-core/ceria-shell catalysts that achieve high methane conversion rates by maximizing the concentration of active Pd/ceria interfacial sites. Together, these results demonstrate the complex nature of Pd/ceria catalysis, in which strong metal–support interactions lead to the co-existence of multiple surface morphologies with unique catalytic properties.

Each of the possible surface morphologies described above may contribute differently to the catalytic activity of the system, and it is essential to identify surface morphologies that are both *stable* and *active* under the reaction conditions of interest. DFT electronic structure calculations and *ab initio* thermodynamics have been applied together to determine the Pd/ceria surface morphologies that are stable under typical operating conditions and that

provide a low energy path for hydrocarbon oxidation. Ongoing efforts will incorporate atomistic simulations *via* the ReaxFF potential to extend our analysis beyond the computational limits of DFT.

### 4.3.4.2   Effect of Pd on CeO$_2$ Surface Reduction

DFT studies completed in our laboratory examined the nature of oxygen vacancy formation and methane activation over Pd-substituted CeO$_2$(111), (110), and (100) surfaces.[69] The results demonstrate that methane activation and oxygen-vacancy formation are surface reduction processes, and that the substitution of a Pd atom in the ceria lattice greatly affects the energetics of these processes. The removal of a surface oxygen when forming a vacancy in the ceria lattice results in a *single-spin* gap state above the valence, which is attributed to the single occupation of *4f* states on two cerium atoms (shown in Figure 4.10). This is confirmed by a Bader charge analysis demonstrating that oxygen-vacancy formation results in a negative charge transfer to two cerium atoms in the vicinity of the oxygen-vacancy, further corroborating density of states (DOS) data suggesting that the removal of an oxygen results in the reduction of two cerium atoms from Ce^{4+} to Ce^{3+}. Bader charge analysis confirms that a Ce^{4+} to Ce^{3+} reduction occurs adjacent to CH$_3$ and H adsorption sites, thus demonstrating that vacancy formation and methane adsorption are surface reduction processes.

A density of states (DOS analysis) can probe the electronic structure changes that occur during surface reductions. This analysis shows the electronic effect of Pd substitution, as well as demonstrates that both O-vacancy formation and dissociative methane adsorption display similar electronic structure rearrangements. The formation of an oxygen-vacancy in Pd-substituted CeO$_2$(111) results in a spin-paired gap state, in contrast to the single-spin state that appears in clean CeO$_2$(111). Bader charge analysis shows charge accumulation on Pd, confirming that the spin-paired state is the result of a Pd^{4+} reduction to Pd^{2+}. A comparison of the structure of the Pd-substituted CeO$_2$ surface before and after reduction shows that, after reduction, Pd assumes a square planar coordination geometry analogous to that of Pd^{2+} in bulk PdO. This demonstrates that the reduction of Pd-substituted surfaces results in one Pd^{4+} to Pd^{2+} reduction, as opposed to two Ce^{4+} to Ce^{3+} reductions over the clean ceria surface. The dissociative adsorption of methane is also a surface reduction process that portrays similar electronic rearrangements, thus leading to the correlation between oxygen vacancy formation energy and methane adsorption energy shown in Figure 4.11. Generally, a substituted Pd atom serves as a reduction center, and the resultant gap state is lower in energy than the analogous gap state over clean CeO$_2$. This results in lower vacancy formation and methane dissociation energies over Pd-substituted surfaces.

### 4.3.4.3   Stability of Pd/Ceria Surface Morphologies

The DFT method employed, like most QM methods, only applies at zero temperature and pressure, and, correspondingly, cannot evaluate the thermodynamic stability of Pd incorporated surfaces. *Ab initio* thermodynamics must
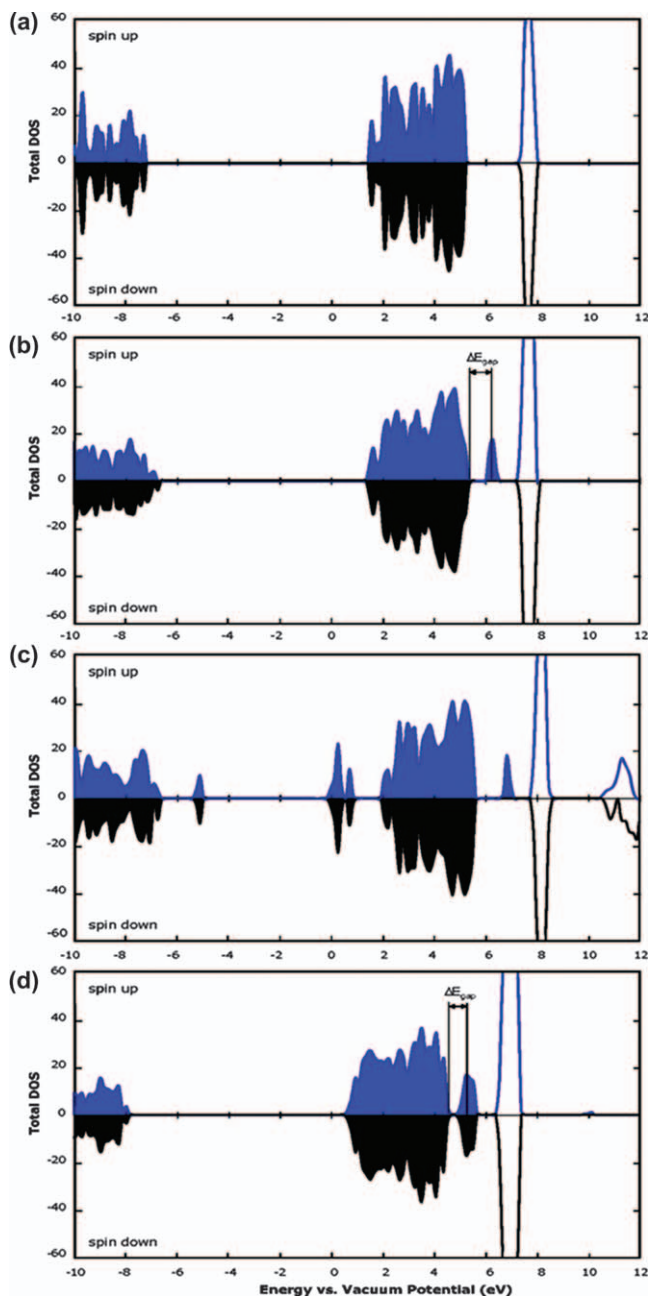
Figure 4.10 Total DOS for (a) clean $CeO_2(111)$, (b) oxygen vacant $CeO_2(111)$, (c) $CeO_2(111)$ with adsorbed *CH_3 and *H, and (d) oxygen vacant Pd-substituted $CeO_2(111)$. Occupied states below the Fermi level are highlighted, and the energy axis is referenced to vacuum potential.
(Reprinted with permission from ref. 69 Copyright 2008 American Chemical Society)

Chapter 4
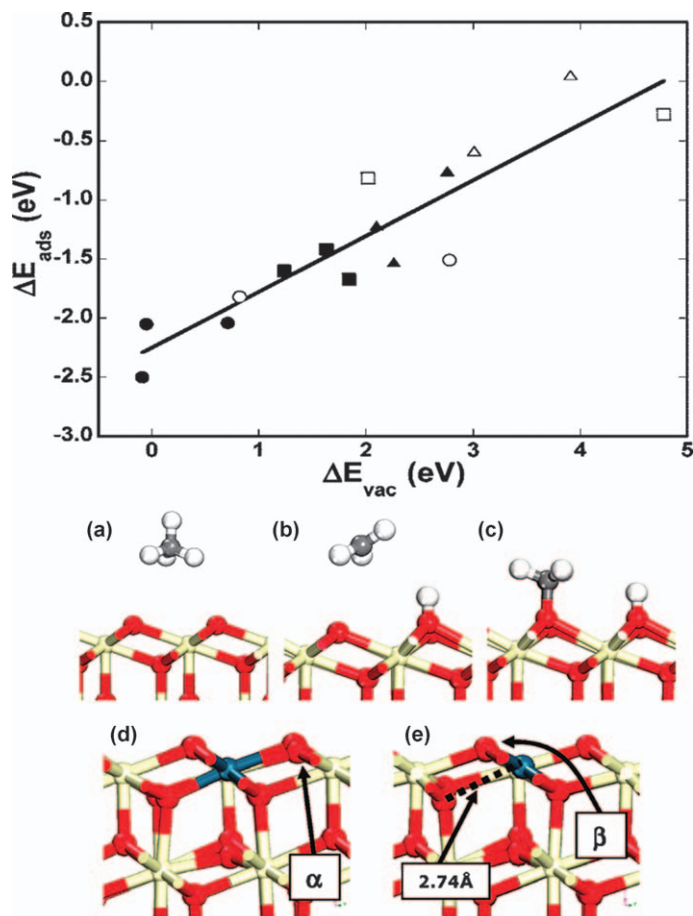
Figure 4.11   Plot demonstrating the correlation between methane adsorption energy, ΔE_{ads}, and oxygen vacancy formation energy, ΔE_{vac}, for Pd-substituted ceria surfaces (●), Zr-substituted surfaces (■), and pure ceria surfaces (▲); open symbols denote pre-reduced surfaces with oxygen vacancies. (a–b) Initial, transition, and final structures for the dissociative adsorption of CH_4 on clean $CeO_2(111)$. (d–e) Structure of Pd-substituted $CeO_2(111)$ before and after oxygen vacancy formation, where α denotes the first oxygen removed and β denotes the second oxygen removed. (Adapted with permission from ref. 69 Copyright 2008 American Chemical Society)

be incorporated to determine the stability of possible Pd/ceria surface morphologies at operating temperatures and pressures. Our laboratory employed such an approach to investigate the stability of single Pd atom states on $CeO_2(111)$, (110), and (100) surfaces.[78] Figure 4.12 contains the resulting phase diagrams showing the temperature and oxygen chemical potential ranges where Pd atoms are stable either: (1) as adsorbed Pd atoms (Pd*), (2) as adsorbed PdO or PdO_2 clusters, or (3) incorporated in Ce lattice positions on either a fully
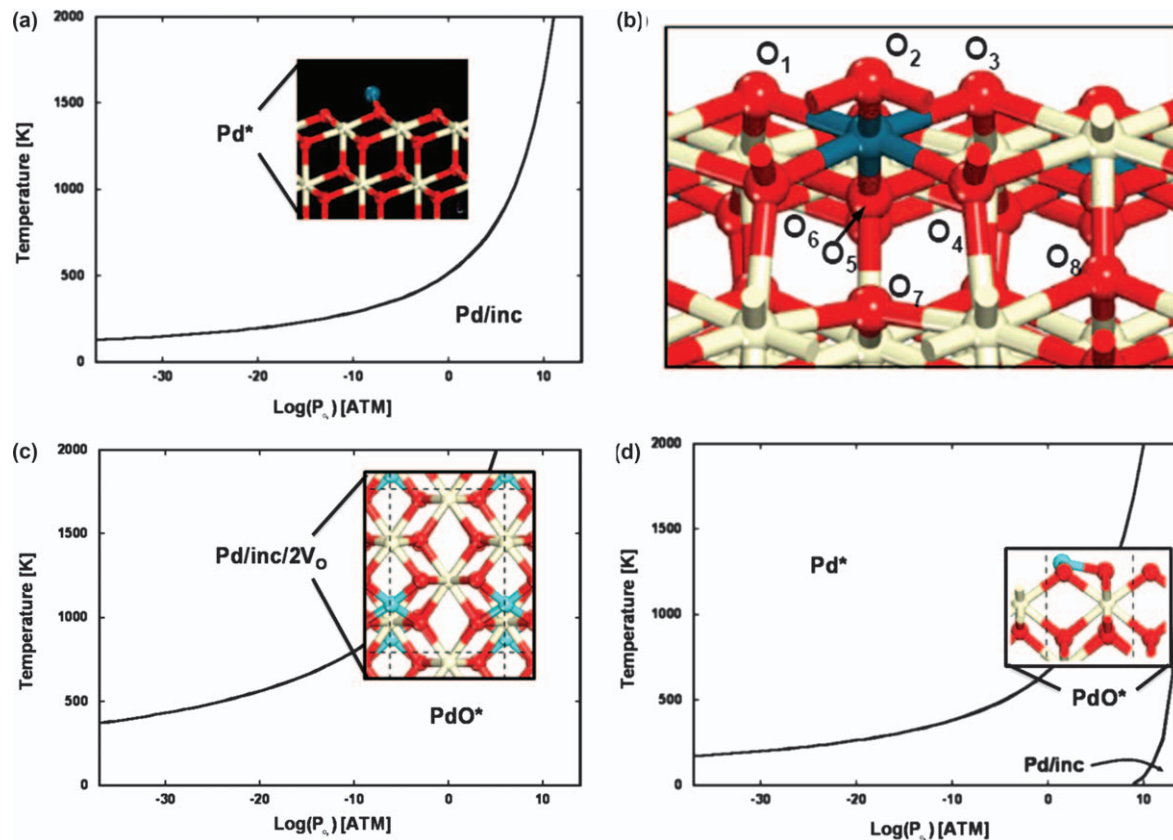
**Figure 4.12** *Ab initio* thermodynamic phase diagrams and insets depicting DFT optimized surface structures for Pd/ceria surface morphologies for (a–b) $CeO_2(111)$, (c) $CeO_2(110)$, and (d) $CeO_2(100)$. (b) Octahedral coordination environment formed by oxygen atoms O1–O6, with O7 moving away from the Pd metal center (compared to O8).
(Adapted with permission from ref. 78 Copyright 2009 American Institute of Physics)

oxidized surface (as Pd^{4+}) or an oxygen deficient surface (as Pd^{2+} or Pd^0). As seen in the figure, each surface is capable of stabilizing an incorporated Pd atom, and the oxidation state of the incorporated Pd atom varies among ceria terminations. For the $CeO_2(111)$ facet, Pd^{4+} ions are thermodynamically stable when incorporated into the fully oxidized surface under high oxygen pressures or low temperatures. The DFT optimized structure of this surface, shown in Figure 4.12(b), demonstrates that Pd-incorporation is stabilized by a surface reconstruction that provides a favorable octahedral oxygen coordination environment for the d^6 metal center. Both oxygen vacancy formation and methane dissociation over this surface cause a restructuring of the surface, providing a square-planar oxygen coordination that stabilizes the d^8 metal center of Pd^{2+}.

Although these studies demonstrate that Pd-incorporation into the CeO_2 surface may be both stable and active for methane dissociation, optimal performance requires activity for the entire catalytic cycle. The high reducibility of the Pd-incorporated surface could alter the free energy landscape of the reaction mechanism so that re-oxidation of the surface becomes rate limiting. To consider this possibility, *ab initio* thermodynamics approaches were used to derive a free energy diagram that takes into account the impact of varying redox conditions (differing CH_4, O_2 and H_2O chemical potentials) on the reaction energy diagram. Figure 4.13 shows the reaction free energy diagram for methane combustion over $CeO_2(111)$ and $Pd_{incorporated}/CeO_2(111)$ surfaces under catalytic combustion conditions. Pd incorporation reduces the reaction energy for each C–H bond activation step, and therefore leads to a faster overall combustion rate. This allows us to conclude that Pd-incorporation is *stable* under combustion conditions and that it lowers the activation barrier of the rate-determining step, making it *active* toward hydrocarbon oxidation.

4.3.4.4 Atomistic ReaxFF of Pd/ceria

Although this previous work has identified a $Pd_xCe_{1-x}O_\delta$ mixed surface oxide as a potentially unique active site, the DFT methods employed are extremely
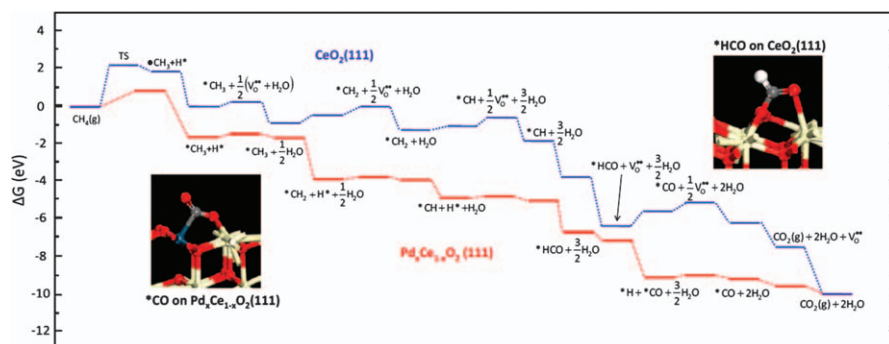
Figure 4.13 Free energy reaction diagrams for complete CH_4 oxidation over (blue) clean $CeO_2(111)$ and (red) Pd-incorporated $Pd_xCe_{1-x}O_\delta$. (Adapted with permission from ref. 89 Copyright 2011 Elsevier)
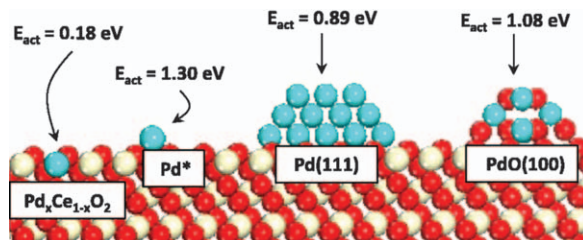
Figure 4.14   DFT-calculated methane activation energies over possible Pd/ceria surface morphologies. Pd-incorporation greatly reduces the C–H bond activation barrier; only highly regular surface structures can be evaluated with DFT.
(Reprinted with permission from ref. 89 Copyright 2011 Elsevier)

limited in the structures that can be considered. Figure 4.14 depicts activation barriers over ordered surface structures that represent limiting cases in which Pd is ideally dispersed throughout the ceria surface, or is entirely contained in pure metal clusters or surface oxides. DFT can only assess these limiting cases separately, and cannot address the combined influence of these separate domains. To model a mixed surface with 2×2 lattice, the surface concentration of Pd atoms is fixed at 25% with Pd atoms incorporated in a specific supercell structure. Lower Pd concentrations, the clustering of Pd dopants, or long range structures involving Pd and O-vacancy clustering are inaccessible with DFT owing to the computational intensity of considering larger supercells. The ReaxFF method will make examination of these possibilities, along with consideration of catalytic reaction chemistry, computationally tractable. As discussed above, the ReaxFF potential is readily suited to handle metal–oxide interfaces under complex hydrocarbon environments. Efforts are currently underway to optimize the ReaxFF potential to treat Ce/Pd/C/O/H systems, and once completed, will be used in tandem with DFT and *ab initio* thermodynamics to determine the combined role of the surface morphologies that were previously only studied as separate limiting cases.

4.4   Conclusions

DFT methods can calculate the ground state electronic structure and energy of a system as a function of nuclear coordinates, allowing one to determine the preferred reaction path by identifying optimal structures on the DFT-calculated potential energy surface (PES). Thus, the utility of DFT lies in its ability accurately to describe the energetics of reactive bond breaking/forming events, which reveals important aspects of the underlying electronic structure, such as oxidation states in atoms, orbital occupancies in molecules, and electronic band structures in solids. *Ab initio* thermodynamics uses statistical mechanics to extend DFT to high temperature and pressure descriptions, which allows one to calculate free energies to assess the stability of the catalyst surface as a function

of chemical environment. Such knowledge is a powerful tool for determining preferred reaction paths over catalytic surfaces, and for building a fundamental understanding of the electronic driving forces behind catalytic mechanisms.

The computational expense of QM limits DFT and *ab initio* thermodynamics to highly idealized models, such as the single crystal surfaces and small clusters considered in the studies above, that only approximate the complex geometry of actual systems. These methods are also limited in their ability to consider dynamic structural transitions at a metal–oxide interface. Although it is difficult to characterize long range and dynamic effects using QM, it becomes possible with the use of empirical force-fields that are based on classical principles and therefore have a relatively low computational expense. The ReaxFF potential is designed to model bond dissociation and formation, and can therefore be implemented in *reactive* molecular dynamics and Monte Carlo simulations that are capable of describing the dynamic nature of a catalyst at longer length and time scales (up to $\sim 10^4$ atoms and ~ 1 ns). Studies utilizing these methods can systematically probe catalytically interesting properties of supported metal–oxide systems that arise from structural irregularities and dynamic effects of surface reconstruction at interfaces.

Together, the computational methods discussed herein allow for a detailed determination of many phenomena influencing the behavior of supported metal–oxide catalysts. The studies considered in this review demonstrate the power of computational methods for assessing the stability and activity of supported metal–oxide catalysts.

References

1. E. Aneggi, C. de Leitenburg, G. Dolcetti and A. Trovarelli, *Catal. Today: Catalytic Control of Diesel Exhaust Emissions*, 2006, **114**, 40–47.
2. R. Burch, P. K. Loader and F. J. Urbano, *Catal. Today*, 1996, **27**, 243–248.
3. L.-H. Xiao, K.-H. Sun, X.-l. Xu and X.-N. Li, *Catal. Commun.*, 2005, **6**, 796–801.
4. S. Colussi, A. Gayen, J. Llorca, C. de Leitenburg, G. Dolcetti and A. Trovarelli, *Ind. Engin. Chem. Res.*, 2012, **51**, 7510–7517.
5. S. Specchia, E. Finocchio, G. Busca, P. Palmisano and V. Specchia, *J. Catal.*, 2009, **263**, 134–145.
6. L. Shi, W. Chu, F. Qu and S. Luo, *Catal. Lett.*, 2007, **113**, 59–64.
7. T. Kuznetsova, V. Sadykov, L. Batuev, E. Moroz, E. Burgina, V. Rogov, V. Kriventsov and D. Kochubey, *J. Nat. Gas Chem.*, 2006, **15**, 149–163.
8. C. Bozo, N. Guilhaume, E. Garbowski and M. Primet, *Catal. Today*, 2000, **59**, 33–45.
9. C. Bozo, N. Guilhaume and J.-M. Herrmann, *J. Catal.*, 2001, **203**, 393–406.
10. M. A. Malecka, L. Kepinski and W. Mista, *Appl. Catal. B: Environ.*, 2007, **74**, 290–298.

11. G. Picasso, M. Gutierrez, M. P. Pina and J. Herguido, *Chem. Engin. J.*, 2007, **126**, 119–130.

12. M. Cargnello, J. J. D. Jaén, J. C. H. Garrido, K. Bakhmutsky, T. Montini, J. J. C. Gámez, R. J. Gorte and P. Fornasiero, *Science*, 2012, **337**, 713–717.

13. G. Jacobs, R. A. Keogh and B. H. Davis, *J. Catal.*, 2007, **245**, 326–337.

14. X. Wang and R. J. Gorte, *Appl. Catal. A: Gen.*, 2002, **224**, 209–218.

15. Q. Zhuang, Y. Qin and L. Chang, *Appl. Catal.*, 1991, **70**, 1–8.

16. E. Nikolla, J. Schwank and S. Linic, *J. Catal.*, 2007, **250**, 85–93.

17. H.-L. Chen, S.-H. Liu and J.-J. Ho, *J. Phys. Chem. B*, 2006, **110**, 14816–14823.

18. Y. Matsumura, W.-J. Shen, Y. Ichihashi and H. Ando, *Catal. Lett.*, 2000, **68**, 181–183.

19. W.-J. S. Y. Matsumura, *Phys. Chem. Chem. Phys.*, 2000, **2**, 1519–1522.

20. A. Yee, S. J. Morrison and H. Idriss, *J. Catal.*, 1999, **186**, 279–295.

21. J. Lahiri, A. Mayernick, S. L. Morrow, B. E. Koel, A. C. T. van Duin, M. J. Janik and M. Batzill, *J. Phys. Chem. C*, 2010, **114**, 5990–5996.

22. H. Idriss, *Platin. Metals Rev.*, 2004, **48**, 105–115.

23. D. Mei, N. A. Deskins, M. Dupuis and Q. Ge, *J. Phys. Chem. C*, 2008, **112**, 4257–4266.

24. D. Mei, N. A. Deskins and M. Dupuis, *Surf. Sci.*, 2007, **601**, 4993–5001.

25. R. Burch, A. Goguet and F. C. Meunier, *Appl. Catal. A: Gen.*, 2011, **409**, 3–12.

26. Y. Chen, H. Wang, R. Burch, C. Hardacre and P. Hu, *Faraday Disc.*, 2011, **152**, 121–133.

27. A. Goguet, F. C. Meunier, D. Tibiletti, J. P. Breen and R. Burch, *J. Phys. Chem. B*, 2004, **108**, 20240–20246.

28. C. M. Y. Yeung, F. Meunier, R. Burch, D. Thompsett and S. C. Tsang, *J. Phys. Chem. B*, 2006, **110**, 8540–8543.

29. G. Jacobs and B. H. Davis, *Appl. Catal. A: Gen.*, 2005, **284**, 31–38.

30. D. Pierre, W. Deng and M. Flytzani-Stephanopoulos, *Topics Catal.*, 2007, **46**, 363–373.

31. X. G. Wang and R.J. Wagner, *J. Catal.*, 2002, **212**, 225–230.

32. X. Wang, J. A. Rodriguez, J. C. Hanson, D. Gamarra, A. Martinez-Arias and M. Fernandez-Garcia, *J. Phys. Chem. B*, 2006, **110**, 428–434.

33. C.-H. Lin, C.-L. Chen and J.-H. Wang, *J. Phys. Chem. C*, 2011, **115**, 18582–18588.

34. R. Burch, *Phys. Chem. Chem. Phys.*, 2006, **8**, 5483–5500.

35. T. Bunlesin, E. S. Putna and R. J. Gorte, *Catal. Lett.*, 1996, **41**, 1–5.

36. M. Boaro, C. de Leitenburg, G. Dolcetti and A. Trovarelli, *J. Catal.*, 2000, **193**, 338–347.

37. D. Teschner, A. Wootsch, O. Pozdnyakova-Tellinger, J. Krohnert, E. M. Vass, M. Havecker, S. Zafeiratos, P. Schnorch, P. C. Jentoft, A. Knop-Gericke and R. Schlogl, *J. Catal.*, 2007, **249**, 318–327.

38. V. Shapovalov and H. Metiu, *J. Catal.*, 2007, **245**, 205–214.

39. S. H. Oh and G. B. Hoflund, *J. Phys. Chem. A*, 2006, **110**, 7609–7613.

40. H. Wang and W. F. Schneider, *Catal. Today*, 2011, **165**, 49–55.

41. R. B. Getman and W. F. Schneider, *ChemCatChem*, 2010, **2**, 1450–1460.

42. W.-J. Zhu, J. Zhang, X.-Q. Gong and G. Lu, *Catal. Today*, 2011, **165**, 19–24.

43. H. W. Jen, G. W. Graham, W. Chun, R. W. McCabe, J. P. Cuif, S. E. Deutsch and O. Touret, *Catal. Today*, 1999, **50**, 309–328.

44. G. W. Graham, H. W. Jen, R. W. McCabe, A. M. Straccia and L. P. Haack, *Catal. Lett.*, 2000, **67**, 99–105.

45. E. Aneggi, M. Boaro, C. D. Leitenburg, G. Dolcetti and A. Trovarelli, *J. Alloy. Comp.*, 2006, **408–412**, 1096–1102.

46. A. Trovarelli, C. D. Leitenburg, M. Boaro and G. Dolvetti, *Catal. Today*, 1999, **50**, 353–367.

47. M. K. Debe, *Nature*, 2012, **486**, 43–51.

48. S. McIntosh, J. M. Vohs and R. J. Gorte, *Electrochem. Solid-State Lett.*, 2003, **6**, A240–A243.

49. S. McIntosh and R. J. Gorte, *Chem. Rev.*, 2004, **104**, 4845–4865.

50. R. J. Gorte, J. M. Vohs and S. McIntosh, *Solid State Ion.*, 2004, **175**, 1–6.

51. S. An, C. Lu, W. L. Worrell, R. J. Gorte and J. M. Vohs, *Solid State Ion.*, 2004, **175**, 135–138.

52. M. Gong, X. Liu, J. Trembly and C. Johnson, *J. Power Sourc.*, 2007, **168**, 289–298.

53. J.-H. Wang, M. Liu and M. C. Lin, *Solid State Ion.*, 2006, **177**, 939–947.

54. A. Borodziński and G. C. Bond, *Catal. Rev.*, 2008, **50**, 379–469.

55. A. Borodziński and G. C. Bond, *Catal. Rev.*, 2006, **48**, 91–144.

56. M. Boronat, F. Illas and A. Corma, *J. Phys. Chem. A*, 2009, **113**, 3750–3757.

57. P. Concepción, S. Carrettin and A. Corma, *Appl. Catal. A: Gen.*, 2006, **307**, 42–45.

58. N. Khan, S. Shaikhutdinov and H. Freund, *Catal. Lett.*, 2006, **108**, 159–164.

59. W. Ludwig, A. Savara, K.-H. Dostert and S. Schauermann, *J. Catal.*, 2011, **284**, 148–156.

60. M. W. Tew, M. Janousch, T. Huthwelker and J. A. van Bokhoven, *J. Catal.*, 2011, **283**, 45–54.

61. Z.-P. Liu and P. Hu, *J. Am. Chem. Soc.*, 2003, **125**, 1958–1967.

62. G. Jacobs, S. Ricote, U. M. Graham, P. M. Patterson and B. H. Davis, *Catal. Today*, 2005, **106**, 259–264.

63. J. H. Holles, R. J. Davis, T. M. Murray and J. M. Howe, *J. Catal.*, 2000, **195**, 193–206.

64. J. A. Farmer and C. T. Campbell, *Science*, 2010, **329**, 933–936.

65. G. B. Hoflund, H. A. E. Hagelin, J. F. Weaver and G. N. Salaita, *Appl. Surf. Sci.*, 2003, **205**, 102–112.

66. W.-J. Shen and Y. Matsumura, *J. Molec. Catal. A: Chem.*, 2000, **153**, 165–168.

67. H. Gabasch, K. Hayek, B. Klötzer, W. Unterberger, E. Kleimenov, D. Teschner, S. Zafeiratos, M. Hävecker, A. Knop-Gericke, R. Schlögl,

B. Aszalos-Kiss and D. Zemlyanov, *J. Phys. Chem. C*, 2007, **111**, 7957–7962.

68. S. Laursen and S. Linic, *J. Phys. Chem. C*, 2009, **113**, 6689–6693.
69. A. D. Mayernick and M. J. Janik, *J. Phys. Chem. C*, 2008, **112**, 14955–14964.
70. H. Borchert, Y. Borchert, V. V. Kaichev, I. P. Prosvirin, G. M. Alikina, A. I. Lukashevich, V. I. Zaikovskii, E. M. Moroz, E. A. Paukshtis, V. I. Bukhtiyarov and V. A. Sadykov, *J. Phys. Chem. B*, 2005, **109**, 20077–20086.
71. Z.-P. Liu, S. J. Jenkins and D. A. King, *Phys. Rev. Lett.*, 2005, **94**, 196102.
72. Z. Yang, G. Luo, Z. Lu, T. K. Woo and K. Hermansson, *J. Phys.: Cond. Matt.*, 2008, **20**, 035210.
73. L. Szabova, M. F. Camellone, M. Huang, V. Matolin and S. Fabris, *J. Chem. Phys.*, 2010, **133**, 234705–234711.
74. M. Nolan, S. Grigoleit, D. C. Sayle, S. C. Parker and G. W. Watson, *Surf. Sci.*, 2005, **576**, 217–229.
75. M. Nolan, S. C. Parker and G. W. Watson, *Surf. Sci.*, 2005, **595**, 223–232.
76. S. Bernal, J. J. Calvino, M. A. Cauqui, J. M. Gatica, C. Larese, J. A. Perez Omil and J. M. Pintado, *Catal. Today*, 1999, **50**, 175–206.
77. B. Wang, D. Weng, X. Wu and J. Fan, *Catal. Today*, 2010, **153**, 111–117.
78. A. D. Mayernick and M. J. Janik, *J. Chem. Phys.*, 2009, **131**, 084701–084712.
79. K. Reuter, D. Frenkel and M. Scheffler, *Phys. Rev. Lett.*, 2004, **93**, 116105.
80. J. F. Weaver, J. A. Hinojosa Jr, C. Hakanoglu, A. Antony, J. M. Hawkins and A. Asthagiri, *Catal. Today*, 2011, **160**, 213–227.
81. H. Zhang, J. Gromek, G. Fernando, H. Marcus and S. Boorse, *J. Phase Equilib. Diffus.*, 2002, **23**, 246–248.
82. J. Rogal, K. Reuter and M. Scheffler, *Phys. Rev. B*, 2004, **69**, 075421.
83. J. Klikovits, E. Napetschnig, M. Schmid, N. Seriani, O. Dubay, G. Kresse and P. Varga, *Phys. Rev. B*, 2007, **76**, 045405.
84. J. A. Rodriguez, X. Wang, J. C. Hanson, G. Liu, A. Iglesias-Juez and M. Fernandez-Garcia, *J. Chem. Phys.*, 2003, **119**, 5659–5669.
85. X. Wang, J. A. Rodriguez, J. C. Hanson, D. Gamarra, A. Martinez-Arias and M. Fernandez-Garcia, *J. Phys. Chem. B*, 2005, **109**, 19595–19603.
86. G. Zhou, P. R. Shah, T. Kim, P. Fornasiero and R. J. Gorte, *Catal. Today*, 2007, **123**, 86–93.
87. S. Colussi, A. Gayen, M. F. Camellone, M. Boaro, J. Llorca, S. Fabris and A. Trovarelli, *Ange. Chem. Int.*, 2009, **48**, 8481–8484.
88. L. M. Misch, J. A. Kurzman, A. R. Derk, Y.-I. Kim, R. Seshadri, H. Metiu, E. W. McFarland and G. D. Stucky, *Chem. Mat.*, 2011, **23**, 5432–5439.
89. A. D. Mayernick and M. J. Janik, *J. Catal.*, 2011, **278**, 16–25.
90. M. L. Drummond, B. G. Sumpter, W. A. Shelton and J. Z. Larese, *J. Phys. Chem. C*, 2007, **111**, 966–976.
91. R. B. Getman, Y. Xu and W. F. Schneider, *J. Phys. Chem. C*, 2008, **112**, 9559–9572.

92. H. Wang and W. F. Schneider, *J. Chem. Phys.*, 2007, **127**, 064706.
93. D. R. Mullins and S. H. Overbury, *Surf. Sci.*, 2002, **511**, L293–L297.
94. J. K. Norskov, T. Bligaard, J. Rossmeisl and C. H. Christensen, *Nat. Chem.*, 2009, **1**, 37–46.
95. P. Hohenberg and W. Kohn, *Phys. Rev.*, 1964, **136**, B864–B871.
96. W. Kohn and L. J. Sham, *Phys. Rev.*, 1965, **140**, A1133–A1138.
97. W. Kohn, A. D. Becke and R. G. Parr, *J. Phys. Chem.*, 1996, **100**, 12974–12980.
98. D. S. Sholl and J. A. Steckel, *Density Functional Theory: A Practical Introduction*, John Wiley & Sons, Inc., 2009; pp 1–233.
99. C. Stampfl, *Catal. Today*, 2005, **105**, 17–35.
100. K. Reuter and M. Scheffler, *Phys. Rev. B*, 2001, **65**, 035406.
101. K. Reuter and M. Scheffler, *Phys. Rev. B*, 2003, **68**, 045407.
102. K. Reuter and M. Scheffler, *Phys. Rev. Lett.*, 2003, **90**, 046103.
103. A. C. T. van Duin, S. Dasgupta, F. Lorant and W. A. Goddard, *J. Phys. Chem. A*, 2001, **105**, 9396–9409.
104. M. Moseler, M. Walter, B. Yoon, U. Landman, V. Habibpour, C. Harding, S. Kunz and U. Heiz, *J. Am. Chem. Soc.*, 2012, **134**, 7690–7699.
105. B. Yoon, H. Häkkinen, U. Landman, A. S. Wörz, J.-M. Antonietti, S. Abbet, K. Judai and U. Heiz, *Science*, 2005, **307**, 403–407.
106. L. M. Molina and B. Hammer, *Phys. Rev. Lett.*, 2003, **90**, 206102.
107. L. M. Molina, M. D. Rasmussen and B. Hammer, *J. Chem. Phys.*, 2004, **120**, 7673–7680.
108. G. P. Petrova, G. N. Vayssilov and N. Rösch, *J. Phys. Chem. C*, 2007, **111**, 14484–14492.
109. P. S. Petkov, G. P. Petrova, G. N. Vayssilov and N. Rösch, *J. Phys. Chem. C*, 2010, **114**, 8500–8506.
110. C. H. Hu, C. Chizallet, C. Mager-Maury, M. Corral-Valero, P. Sautet, H. Toulhoat and P. Raybaud, *J. Catal.*, 2010, **274**, 99–110.
111. C. Mager-Maury, G. Bonnard, C. Chizallet, P. Sautet and P. Raybaud, *ChemCatChem*, 2011, **3**, 200–207.
112. R. Ferrando, G. Rossi, F. Nita, G. Barcaro and A. Fortunelli, *ACS Nano*, 2008, **2**, 1849–1856.
113. G. Barcaro and A. Fortunelli, *J. Phys. Chem. C*, 2007, **111**, 11384–11389.
114. G. Barcaro, A. Fortunelli, G. Granozzi and F. Sedona, *J. Phys. Chem. C*, 2009, **113**, 1143–1146.
115. J. A. Rodriguez, P. Liu, J. Hrbek, J. Evans and M. Pérez, *Ange. Chem. Int. Ed.*, 2007, **46**, 1329–1332.
116. J. A. Rodriguez, S. Ma, P. Liu, J. Hrbek, J. Evans and M. Pérez, *Science*, 2007, **318**, 1757–1760.
117. A. Bruix, J. A. Rodriguez, P. J. Ramírez, S. D. Senanayake, J. Evans, J. B. Park, D. Stacchiola, P. Liu, J. Hrbek and F. Illas, *J. Am. Chem. Soc.*, 2012, **134**, 8968–8974.
118. C. Zhang, A. Michaelides and S. J. Jenkins, *Phys. Chem. Chem. Phys.*, 2011, **13**, 22–33.

119. P. Liu and J. A. Rodriguez, *J. Chem. Phys.*, 2007, **126**, 164705–164708.
120. J. A. Rodriguez and F. Illas, *Phys. Chem. Chem. Phys.*, 2012, **14**, 427–438.
121. X. Wang, J. A. Rodriguez, J. C. Hanson, M. Perez and J. Evans, *J. Chem. Phys.*, 2005, **123**, 221101–221105.
122. R. F. W. Bader, *Acc. Chem. Res.*, 1985, **18**, 9–15.
123. Y. Chen, J. Cheng, P. Hu and H. Wang, *Surf. Sci.*, 2008, **602**, 2828–2834.
124. S. C. Ammal and A. Heyden, *J. Phys. Chem. C*, 2011, **115**, 19246–19259.
125. S. C. Ammal and A. Heyden, *J. Phys. Chem. C*, 2011, **116**, 1624–1624.
126. T. Ishida, N. Kinoshita, H. Okatsu, T. Akita, T. Takei and M. Haruta, *Ange. Chem. Int. Ed.*, 2008, **47**, 9265–9268.
127. Z. Zhou, S. Kooi, M. Flytzani-Stephanopoulos and H. Saltsburg, *Adv. Funct. Mat.*, 2008, **18**, 2801–2807.
128. S. Aranifard, S. C. Ammal and A. Heyden, *J. Phys. Chem. C*, 2012, **116**, 9029–9042.
129. W. A. Goddard, J. E. Mueller and A. C. T. van Duin, *J. Phys. Chem. C*, 2010, **114**, 4939–4949.
130. J. E. Mueller, A. C. T. van Duin and W. A. Goddard, *J. Phys. Chem. C*, 2010, **114**, 5675–5685.
131. K. Chenoweth, A. C. T. van Duin, P. Persson, M.-J. Cheng, J. Oxgaard and I. I. I. W. A. Goddard, *J. Phys. Chem. C*, 2008, **112**, 14645–14654.
132. K. Chenoweth, A. C. T. van Duin and W. A. Goddard III, *Ange. Chem. Int.*, 2009, **48**, 7630–7634.
133. N. Metropolis, A. W. Rosenbluth, M. N. Rosenbluth, A. H. Teller and E. Teller, *J. Chem. Phys.*, 1953, **21**, 1087–1092.
134. P. A. Deshpande, M. S. Hegde and G. Madras, *AIChE J.*, 2010, **56**, 1315–1324.